Hollow-waveguide tri-band shared-aperture full-corporate-feed continuous transverse stub antenna

You, Qingchun; Lu, Yunlong; Wang, Yi; Xu, Jun; Huang, Jifu; Hong, Wei

DOI:
10.1109/TAP.2022.3161265

Hollow-Waveguide Tri-Band Shared-Aperture Full-Corporate-Feed Continuous Transverse Stub Antenna

Qingchun You, Yunlong Lu, *Member, IEEE,* Yi Wang, *Senior Member,* Jun Xu, *Member, IEEE,* Jifu Huang, and Wei Hong, *Fellow, IEEE*

***Abstract*— This paper presents a tri-band shared-aperture full-corporate-feed continuous transverse stub (CTS) antenna based on hollow-waveguide. The multi-band operation is enabled by a broadband CTS radiator and a novel 6-port parallel-plate waveguide (PPW) multiplexer. The CTS radiation slot is fed by a broadband vertical PPW power divider. The 6-port multiplexer is composed of three diplexers, which defines the three frequency bands – Ku, K, and Ka. The quasi-TEM mode in the PPW structure is generated by single-layer linear source generators (LSGs). Four such LSGs operating at three different bands are used to feed into the multiplexer. The amplitude and phase pre-compensation method is applied in the LSG to overcome the imbalance and spurious reflection caused by the metal walls at the terminal ends of the PPW. This has resulted in improved radiation performance in all three bands. A prototype antenna is designed, fabricated and measured. Good agreement between simulation and measurement has been shown. The peak gains of the antenna over the frequency range of 11.25-15 GHz, 17.7-22 GHz and 27.5-32 GHz are better than 24.7 dBi, 28.2 dBi and 32.1 dBi, respectively. Over 80% antenna efficiency has been achieved in all three frequency bands.**

Keywords—*Continuous transverse stub (CTS) antenna, tri-band, shared-aperture, high-gain, line source generator.*

I. INTRODUCTION

Wireless communications have commonly moved towards multi-band and multi-function operation [1]-[3]. Examples are the 28 GHz (26.5 - 29.5 GHz) and 38 GHz (37 - 40 GHz) bands for 5G millimeter-wave (mmW) communication, and the Ku-band (12.25-12.75 GHz and 14-14.5 GHz), K- (17.7-21.2 GHz) and Ka-bands (27.5-31 GHz) for satellite communication [4]-[6]. High gain array antennas are preferred to establish stable communication links over a long distance. Due to the large frequency band span, increasingly multiple antennas operating in different frequencies are used on the same platform [7]-[10]. This inevitably increases the complexity and the form factor of the antenna system. Therefore, it would be highly desirable if the multiple antennas for different frequency bands can be merged into the same aperture [11], [12]. In this way, the number of antennas is reduced while the aperture reuse efficiency is enhanced.

Conventionally, the planar multi-band shared-aperture antennas are mostly based on microstrip line and operate below Ku-band [13]-[17]. This is because, as the frequency rises further, the limited spacing between antenna elements deteriorates the isolation. Meanwhile, the increased insertion loss and unwanted parasitic radiation associated with the microstrip line lower the antenna efficiency. Recent efforts have seen mmW shared-aperture array antennas based on substrate-integrated waveguide (SIW) technology [18]-[23]. For example, a SIW-based Ku/Ka-band shared-aperture array antenna for beam-scanning application was presented in [22]. In [23], the structure-reuse technology was applied to shared-aperture antenna with an extremely large frequency ratio. The structure is a merge of a slot array and a patch antenna supports radiation at 3.5 GHz and 60 GHz. However, the frequency ratios in the previous work [22], [23] are restricted by the antenna topology and may not be flexibly controlled. Meanwhile, the dielectric loss from the SIW structure is not trivial. An alternative method to the shared-aperture array antenna is using separate feeding networks to excite the same slot array. The frequency ratio can be more flexibly designed. The works [24] and [25] employed air-filled gap waveguide to realize a high-efficiency K/Ka dual-band array antenna. Its frequency ratio, however, is limited by the bandwidth of the slot array. Unacceptable grating lobs may appear at the higher frequency bands due to the larger element spacing [25].

Continuous transverse stub (CTS), for its ultra-wideband and high-efficiency characteristic, has been used in various mmW high-performance antenna applications, such as fixed-beam [26]-[29], multi-beam [30] and beaming-scanning [31]-[35].

This work was supported partly by National Key R&D Program of China under Project 2018YFB1802100, in part by National Natural Science Foundation of China under Projects 62171242, 61801252, U1809203, and 61631012, in part by Zhejiang Provincial Natural Science Foundation of China under Project LY21F010002, and LQ21F010005, Guangdong R&D Project in Key Areas under grant no. 2019B010156004. (Corresponding author: *Yunlong Lu*)

Qingchun You, Yunlong Lu, and Jifu Huang are with the Faculty of Electrical Engineering and Computer Science, Ningbo University, Ningbo, Zhejiang, 315211, China (e-mail: luyunlong@nbu.edu.cn).

Yi Wang is with School of Engineering, University of Birmingham, B15 2TT, United Kingdom (e-mail: y.wang.1@bham.ac.uk).

Jun Xu is with the State Key Laboratory of Terahertz and Millimeter Waves, Department of Electrical Engineering, City University of Hong Kong, Hong Kong SAR, China.

W. Hong is with the State Key Laboratory of Millimeter Waves, School of Information Science and Engineering, Southeast University, Nanjing, 210096, China.

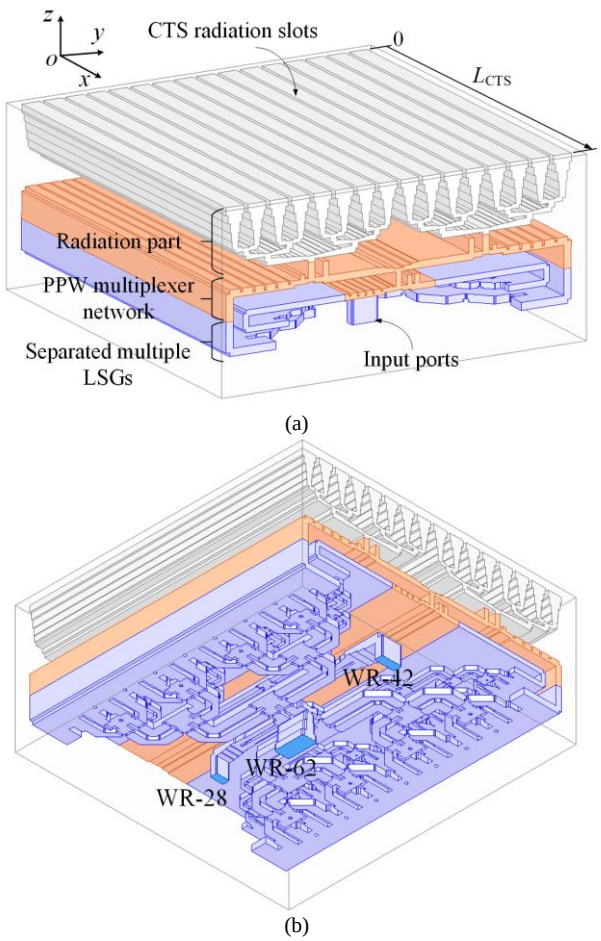

Fig. 1. Three-dimensional view of the air model of the proposed CTS antenna. (a) Front view; (b) back view.

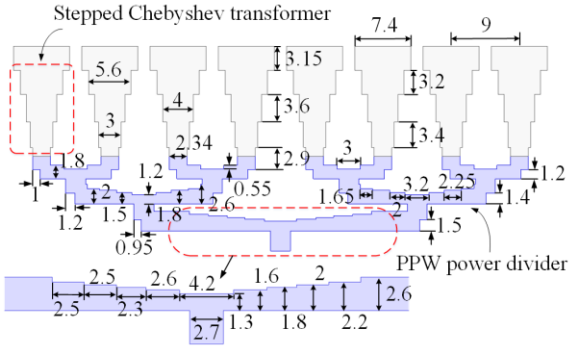

Fig. 2. Cross-sectional view of half of the CTS radiation slots and the vertical PPW power divider. All dimensions are given in millimeters.

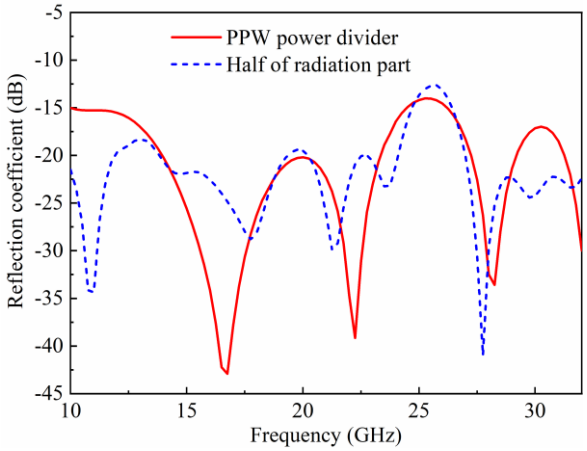

Fig. 3. Simulated reflection coefficients for the 1-to-8 PPW power divider alone and for half of the whole radiation part.

Wideband linear source generator (LSG) and full-corporate-feed parallel plate waveguide (PPW) power divider, as the feed network, is commonly used to support the wideband of CTS antenna. So far, the reported maximum fractional bandwidth of the CTS antenna is around 48% [36], which can not perfectly cover the aforementioned multiple bands of 5G or satellite communication. Utilizing a dual-/multi-band CTS antenna has become an alternative way. Recently, a dual-band shared-aperture variable inclination CTS (VICTS) was reported in [37]. Two independent feed networks at K- and Ka-bands were used to excite a shared radiation slots in series for beam steering. Very narrow bandwidths of 3.0% (K-band) and 2.7% (Ka-band) were obtained. To the best of our knowledge, there is no published work concerning full-corporate-feed multi-band shared- aperture CTS antenna.

This work aims to demonstrate a design methodology for a tri-band shared-aperture full-corporate-feed CTS antenna. A new PPW diplexer based on low-pass and band-stop filters is proposed to separate the quasi-TEM waves for the CTS into different bands. A 6-port multiplexer network, composed of three diplexers, is excited by separated LSGs to achieve the tri-band shared-aperture operation. With the help of an ultra-wideband CTS structure, the frequency ratios between the three bands are determined by the multiplexer and LSGs. Very importantly, this allows more flexible control of the frequency bands. As an additional feature of the design, amplitude and phase pre-compensation technology is used in the LSG to improve the radiation performance in the three bands. The paper is organized as follows: Section II describes the antenna configuration. Section III and IV present the antenna analysis, design, and results followed by the conclusion in Section V.

II. Antenna Configuration

The tri-band CTS antenna covers 11.25-15 GHz (Ku-band), 17.7-22 GHz (K-band), and 27.5-32 GHz (Ka-band). Its configuration is shown in Fig. 1. It consists of three parts: the radiation part, the PPW multiplexer network, and multiple separate LSGs. The whole structure is based on hollow-waveguide (HW) to maximise the gain and antenna efficiency. The functions of the constituent parts are introduced here, whereas the design details will be given in the following sections. The radiation part consists of 16 CTS radiation slots and two vertical PPW 1-to-8 power dividers. The CTS radiation slot supports wideband operation to cover all three frequency bands. The PPW dividers deliver wideband, equal-amplitude and in-phase outputs, feeding into the radiation slots. Three PPW diplexers form the multiplexer network, which defines the signal paths for the three operating frequency bands. To generate the quasi-TEM wave in the PPW structures, multiple separate LSGs are used. Three standard waveguide input ports (WR-62 for Ku-band, WR-42 for K-band and WR-28 for Ka-band) are located at the back side of antenna. By changing

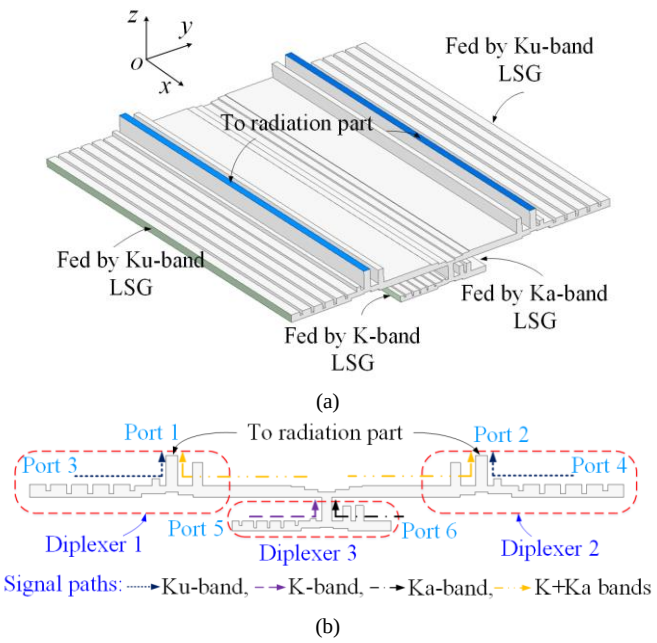

Fig. 4. Configuration of the proposed multiplexer. (a) 3-D view; (b) schematic.

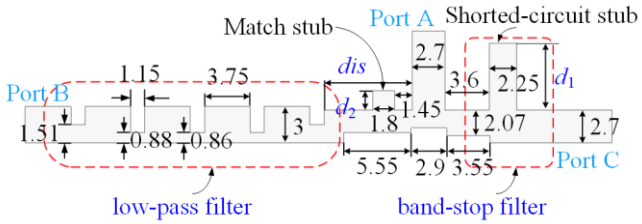

Fig. 5. Structure of Diplexer 1(2). All dimensions are given in millimeters.

the channel operating frequencies of the multiplexer and the corresponding LSGs, the frequency ratio of the antenna can be flexibly adjusted. All the simulation results are carried out using Ansoft HFSS. The design details for each component will be presented next.

III. Analysis and Design

A. CTS Radiation Slots and PPW Power Divider

Starting with the radiation part, it should have broadband characteristics to cover the required three frequency bands. Fig. 2 shows half of the radiation part. The period of the CTS radiation slots is 9 mm, less than the free-space wavelength at the maximum operating frequency, so that the grating lobes can be suppressed in all frequency bands. A stepped Chebyshev transformer inspired by [38] is employed in the radiation slot to allow wide impedance bandwidth between the output of the vertical PPW power divider and free space. The total width (*y*-direction) of the 16 CTS radiation slots is 142.4 mm. The length of the radiation slot (L_{CTS}) is equal to the width of LSG. In order to realize a quasi-square antenna aperture, the width of LSG is set to 150 mm, including the width of termination offsets (see in Section III-C). To support the wideband CTS radiation slots, the PPW T-junction should also have wide bandwidth. This is also achieved by multiple stepped impedance transformers. Based on the optimized dimensions shown in Fig. 2, the reflection coefficients for the 1-to-8 power

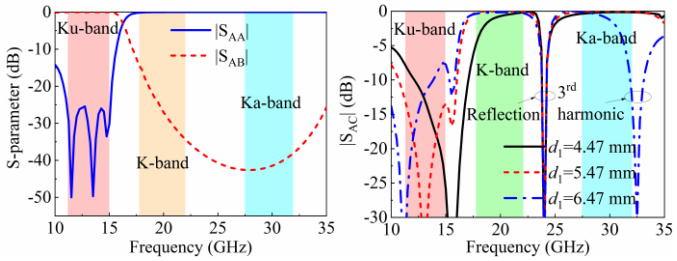

Fig. 6. Simulated S-parameters in Diplexer 1(2): (a) low-pass filter responses and (b) $|S_{AC}|$ in band-stop filter with different lengths of the shorted-circuit PPW stub.

divider alone and for half of the whole radiation part are shown in Fig. 3. They are both below -12 dB over the frequency range of 10-32 GHz (covering the three target frequency bands).

B. PPW multiplexer

With the above-mentioned broadband radiator, there are actually two solutions to achieve the tri-band shared-aperture: (1) The radiation part is excited by a single ultra-wideband LSG (TEM mode), cascaded with a TE-mode waveguide multiplexer to define the three passbands; (2) The radiation part is excited by a PPW (or quasi TEM-mode) multiplexer, cascaded with multiple independent LSGs (including their feed network). Limited to the bandwidth of the LSG, the first solution becomes difficult to realize and therefore the second solution is chosen, which is the antenna structure in Fig. 1.

The key component is the PPW multiplexer, which is used to separate the signal into three operating frequency bands from the common radiator. Fig. 4 shows this novel multiplexer structure, with the different signal paths indicated. This is a 6-port network formed of three PPW diplexers (Diplexers 1, 2, and 3). Ports 1 and 2 of the multiplexer are connected to the inputs of the radiation part (as discussed in Section III-A). Ports 3, 4, 5, and 6 take in the outputs from four separate LSGs operating at Ku-, Ku-, K- and Ka-band, respectively. The basic operating principle of the 6-port multiplexer is: (i) Diplexer 3 combines the K- and Ka-band signals from Port 5 and 6 into its common port, which is then divided equally into two branches. Each is then connected to Diplexer 1 and 2, which are identical. (ii) Diplexer 1 and 2 combine the output from Diplexer 3 with the Ku-band signals from Port 3 or 4 to feed the radiating part of the antenna. The signal path diagram is shown in Fig. 4(b). For ease of understanding, signal paths for different frequency bands are indicated by different colors.

All three diplexers are realized using a PPW T-junction cascaded with a low-pass filter (LPF) and a band-stop filter (BSF). Fig. 5 shows the structure of Diplexer 1 (2), as well as the optimized dimensions. Ports A, B, C are the input/output ports of the Diplexer 1 (2). The LPF is between ports B and A, and the BSF is between ports C and A. The LPF is a 3th-order PPW filter with a Chebyshev response, which allows the Ku-band signal but suppresses the K- and Ka-bands. The simulated results of the LPF are plotted in Fig. 6(a). Its pass-band covers 11.25-15 GHz, whereas the frequency bands of 17.7-22 GHz and 27.5-32 GHz are suppressed by more than 15 dB.

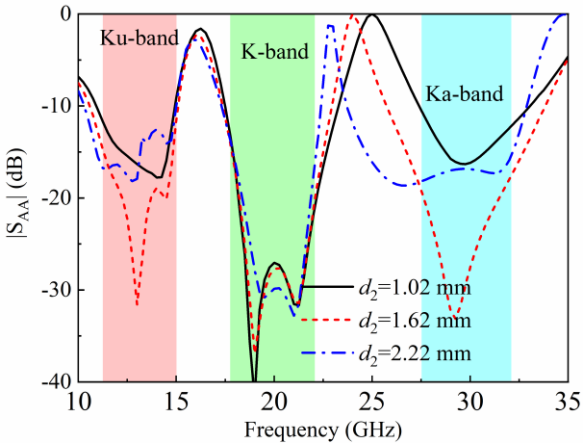

Fig. 7. Simulated $|S_{AA}|$ with different length of match stub (Fig. 5).

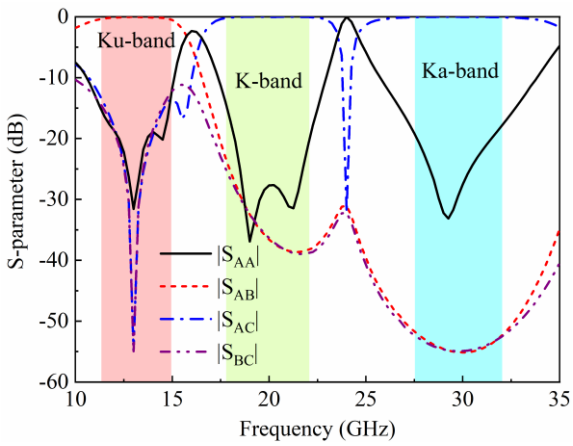

Fig. 8. Simulated S-parameters of Diplexer 1(2).

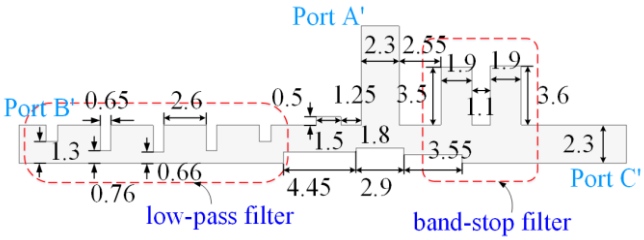

Fig. 9. Structure of Diplexer 3. All dimensions are given in millimeters.

For the K+Ka signal path (between Port C and A in Fig. 5) in Diplexer 1 (2), the Ku-band signal should be suppressed. The truncated PPW in this design, functioned as an oversized waveguide [39], has a very low cut-off frequency. It is about 1 GHz with the PPW aperture sizes of 150 mm × 3 mm. The Ku-band signal suppression is achieved by using an extra loaded quarter-wavelength shorted-circuit PPW stub, as shown in Fig. 5. Fig. 6(b) shows the simulated $|S_{AC}|$ with different lengths of the PPW stub (d_1). When d_1 is 5.47 mm, the BSF has a stop-band rejection of larger than 12 dB over 11.25-15 GHz, while maintaining well matched (over 14 dB return loss) pass-bands over 17.7-22 and 27.5-32 GHz.

An additional matching stub is added to the T-junction close to Port A to improve the impedance matching at all the three frequency bands. By adjusting its height, d_2, the impedance matching can be optimized, as shown in Fig. 7. d_2 is chosen to be 1.62 mm.

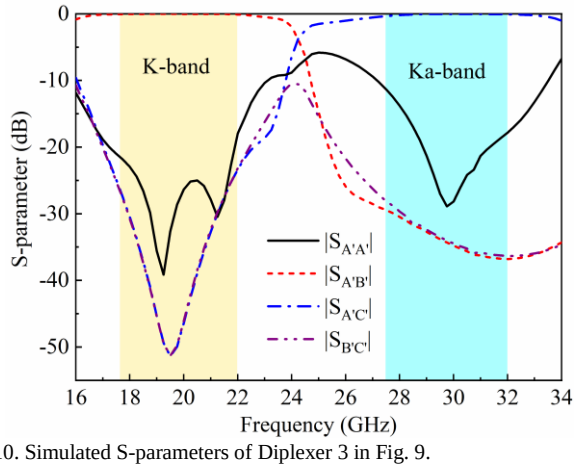

Fig. 10. Simulated S-parameters of Diplexer 3 in Fig. 9.

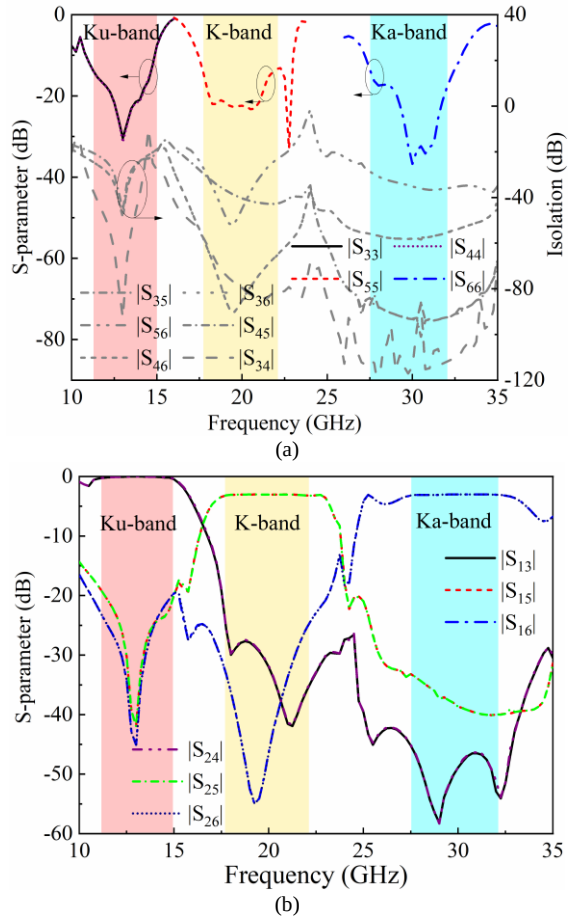

Fig. 11. Simulated results of the proposed 6-port multiplexer (Fig. 4). (a) Reflection coefficients and isolation; (b) transmission coefficients.

Fig. 8 shows the simulated responses of Diplexer 1 (2). In the three frequency bands of interest, the reflection coefficients are all lower than -11 dB. The isolation between the two channels, $|S_{BC}|$, is less than -12 dB over the three frequency bands.

The structure and dimensions of Diplexer 3 are shown in Fig. 9. It has a similar topology as Diplexer 1 (2), except for the BSF. Due to the small guard band between the two channels in Diplexer 3, one more shorted-circuit stub is added to enhance the isolation. The input/output ports in Diplexer 3 are defined as ports A', B' and C'. Fig. 10 plots the simulated results. Over 17.7-22 GHz and 27.5-32 GHz, $|S_{A'A'}|$ is less than -11 dB and

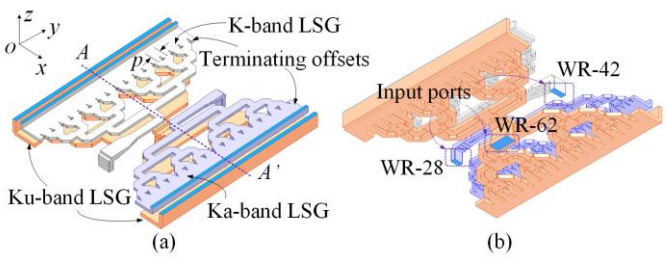

Fig. 12. Layout of the four LSGs: (a) Front and (b) back view.

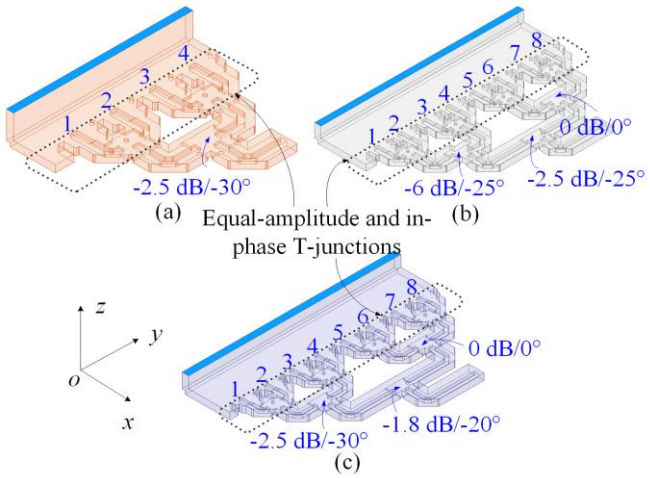

Fig. 13. Layout of each LSG. (a) Ku-band LSG; (b) K-band LSG; (c) Ka-band LSG.

$|S_{B'C'}|$ is less than -20 dB.

Fig. 11 shows the simulated S-parameters of the whole 6-port multiplexer (Fig. 4). The three frequency bands are clearly defined. Ports 3 and 4 support the passband of 11.25-15 GHz, Port 5 supports 17.7-22 GHz, and Port 6 supports 27.5-32 GHz. The reflection coefficients in the three passbands are all lower than -10 dB, and the channel isolations are all better than 20 dB. It should be noted that there is a 3 dB drop in the two upper bands, due to the T-junction power divider at the output of Diplexer 3. The configuration of this multiplexer can be extended to other scales of CTS array antennas. For example, for 8 or less radiating slots, the multiplexer can be reduced. For 32 or more radiating slots, the multiplexer can be remained while the vertical PPW power divider can be modified to feed different numbers of radiation slots.

C. LSGs

The LSG is used to generate quasi-TEM waves to excite the PPW multiplexer, as a TE_{10} to TEM-mode converter. As mentioned in Section II, four LSGs are used: two for Ku-band, one for K-band and Ka-band each. They are all based on multiple-port excited PPW structure [29], [34]. Different from the pillbox-based LSG [27], it only requires a single-layer and has broadband characteristics. This helps reduce the number of vertical metal layers in the CTS antenna.

The arrangement of the four LSGs is shown in Fig. 12. The Ku-band LSG is implemented by using a 1-to-8 power divider, whereas the K- and Ka-band LSGs are based on a 1-to-16 power divider. Only half of each LSG is shown in Fig. 13, according to the symmetry plane *A*-*A*'. It is important to ensure

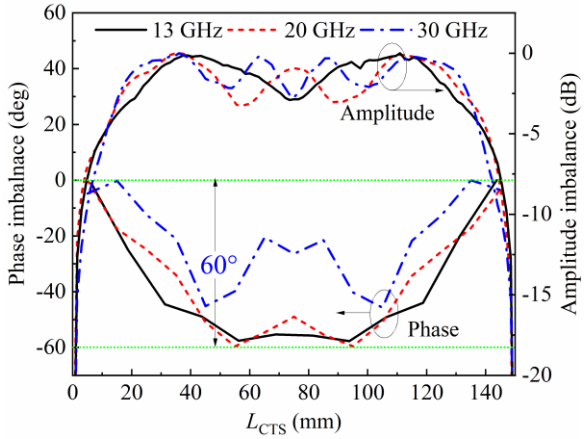

Fig. 14. Simulated uncompensated amplitude and phase distribution of E-field along the radiation slot at different center frequencies.

TABLE I
THE REQUIRED AMPLITUDE AND PHASE DISTRIBUTION AMONG THE OUTPUT PORTS OF THE CORRESPONDING POWER DIVIDER

Port number		1	2	3	4	5	6	7	8
Ku-band	Amp. (dB)	-2.5	-2.5	0	0	--	--	--	--
	Phase (deg)	-30	-30	0	0	--	--	--	--
K-band	Amp. (dB	-6.5	-6.5	-0.5	-0.5	0	0	0	0
	Phase (deg)	-50	-50	-25	-25	0	0	0	0
Ka-band	Amp. (dB)	-3.2	-3.2	-0.7	-0.7	0	0	0	0
	Phase (deg)	-50	-50	-20	-20	0	0	0	0

that the quasi-TEM waves generated by these different LSGs are uniformly distributed in the PPW for optimal antenna efficiency in all three frequency bands. This is achieved by optimizing the space (*p*) between the output ports of the power divider in the LSGs [29]. For the Ku-band, it is 16.5 mm, and for K- and Ka-band, it is 8.8 mm and 9 mm, respectively.

The presence of metal walls on both ends of the PPW adversely affects the amplitude and phase distribution of the quasi-TEM wave near the edges of the PPW [40]. So, two λ/4 terminating offsets are added at both ends to reduce reflections in each LSG (i.e. λ is chosen as the free space wavelength at the center frequency of each band) [29]. Although the reflection from the metal walls is reduce effectively, other remaining reflections are superimposed as the quasi-TEM wave propagates along the PPW. This results in an increase in the imbalance of amplitude and phase distribution. Fig. 14 plots the amplitude and phase distribution of the E-field as a function of the distance L_{CTS} (marked out in Fig. 1) along the CTS radiation slot at the center frequencies of the three frequency bands. It can be seen that the amplitude imbalance exceeds 3.2 dB in all three frequencies. The amplitude also drops rapidly in the regions of around [0, 30] mm and [120, 150] mm. As for the phase, it is in advance near both ends of the radiation slot and the imbalance is up to 60°. When the length of the radiation slot changes, the imbalance regions would still stay near the metal walls of the PPW. These imbalances will decrease the antenna efficiency.

To solve this problem, amplitude and phase compensation features have been added to the conventional power divider in the LSG. The design steps for the pre-compensation are:

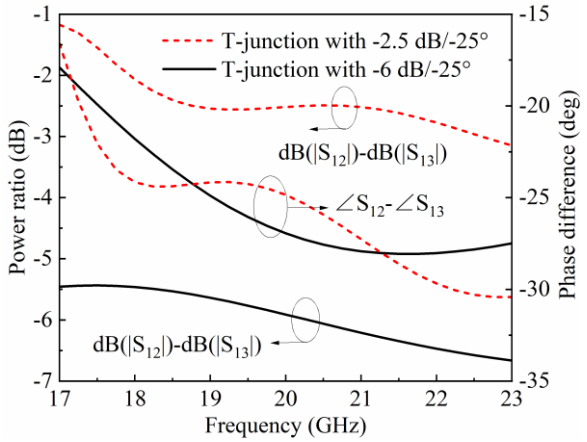

Fig. 15 Amplitude and phase responses of the unequal T-junctions in K-band LSG.

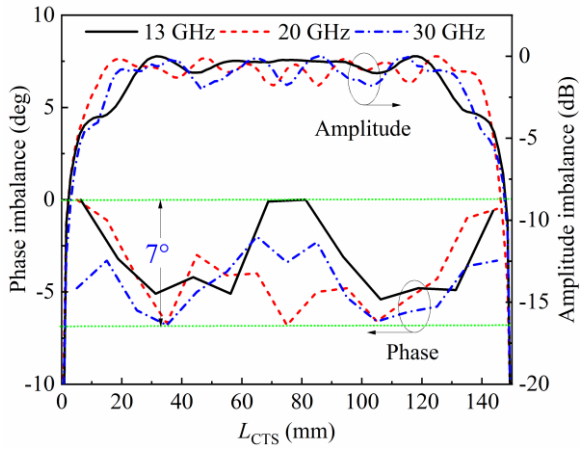

Fig. 16. Simulated amplitude and phase distribution of E-field along the radiation slot with amplitude and phase pre-compensations at different frequencies.

(i) Adjust the phase distribution among the outputs of the power divider at the desired operating frequency to cancel the phase imbalance caused by the metal walls of the PPW.

(ii) Adjust the amplitude distribution of the power divider to further minimize the amplitude imbalance. Repeat step (i) to correct the phase if necessary. After these two steps, the desired amplitude and phase distribution among the output ports of the power dividers are obtained and listed in Table I.

(iii) Establish the required power ratios and phase differences of the corresponding T-junctions in order to meet the phase and amplitude distribution given in Table I. These are given in Fig. 13(a), (b) and (c) and implemented by replacing some of the equal/in-phase T-junctions of the equal/in-phase power divider in the LSG with unequal T-junctions with phase difference.

It is noted that the power ratio and phase difference refers to the amplitude and phase variations between the right and left output ports of the power divider. The detailed design of the unequal T-junction and the phase difference correction method have been reported in [41], and it is not repeated here.

The amplitude and phase imbalances in the unequal T-junctions affect the effective bandwidth of the proposed pre-compensation technology. The larger the required power ratio and phase difference, the narrower the effective fractional

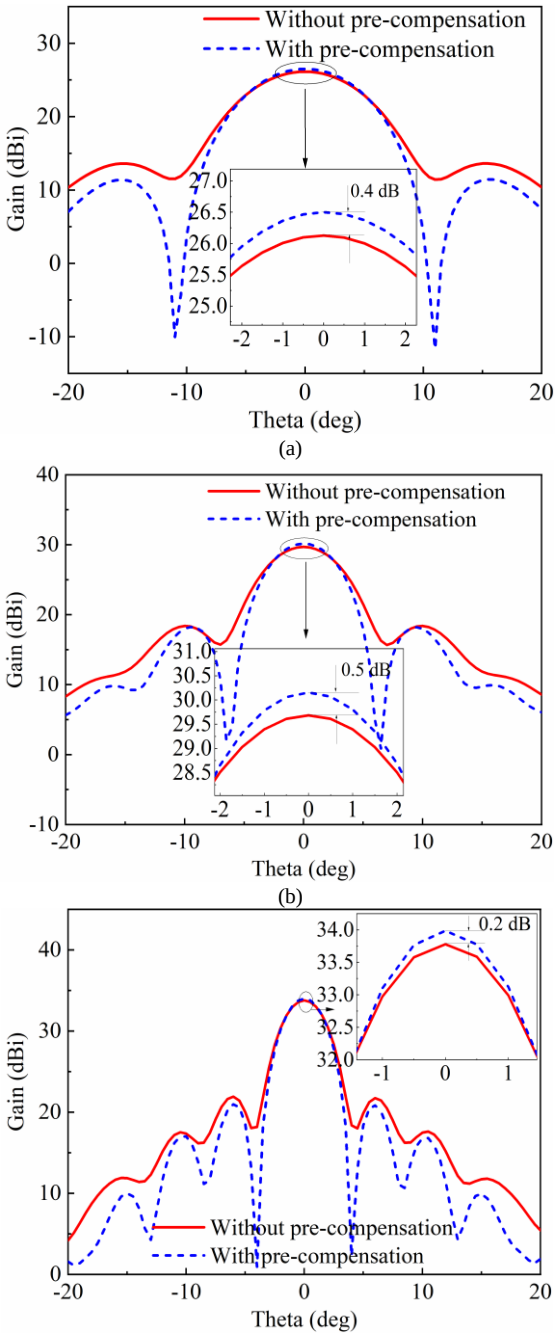

Fig. 17. Simulated radiation patterns with and without amplitude and phase pre-compensation in H-plane. (a) 13 GHz; (b) 20 GHz; (c) 30 GHz.

bandwidth (FBW) of the T-junction. In this work, the maximum power ratio and phase difference occur in the K-band LSG. The amplitude and phase responses of the two T-junctions involved in K-band LSG is shown in Fig. 15. It can be seen that the power ratio and phase difference in the unequal T-junctions are acceptable over the concerned frequency range (17.7-22 GHz). For T-junctions with smaller power ratio and phase difference, the FBW would be wider [41]. The amplitude and phase distribution of the E-field after pre-compensation are shown in Fig. 16. Significantly reduced fluctuations within 2 dB and 7° at the center frequencies of the three bands have been achieved. Moreover, the regions with abrupt amplitude drop

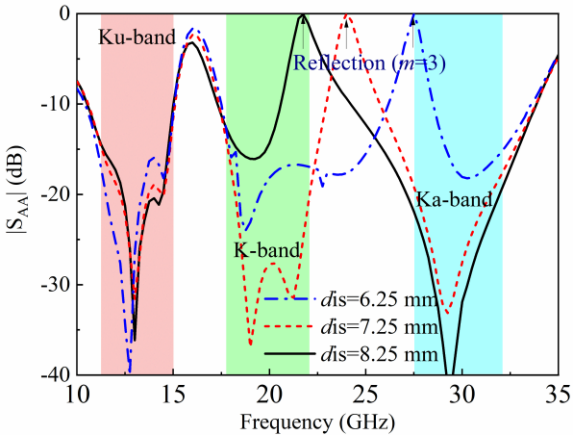

Fig. 18. Simulated $|S_{AA}|$ at port A in Diplexer 1(2) with different values of *dis*.

have been reduced to around [0, 15] mm and [135, 150] mm, further reducing the influence of the metal walls at both ends of the PPW.

The effect of the improved LSG can be seen from the radiation patterns shown in Fig. 17, from the comparison with and without amplitude and phase pre-compensation at 13 GHz, 20 GHz and 30 GHz. It is noted that these results are based on the whole CTS antenna with 16 CTS radiation slots. The peak gain of the antenna is increased by up to 0.5 dB (correspondingly, the antenna efficiency is up by 10%).

If lower SLL is required, the amplitude distributions both in E- and H-planes could be weighed. Due to the significantly decayed amplitude, the reflection from the metal walls at both ends of the PPW is reduced. The amplitude weighting can be performed among the output ports of the power divider to obtain the desired amplitude tapering [34], [42]. This will help realize the low SLL in the H-plane. In the E-plane, this can be achieved by weighing the amplitude distribution of the generated quasi-TEM wave, as demonstrated in [27]. However, the reduced SLL will be at the cost of a reduced antenna efficiency (peak gain).

D. Discussion about achievable frequency ratios

Due to the wideband nature of the PPW-based radiation part and individually designed LSG networks, the frequency ratios of the three frequency bands are largely determined by the 6-port multiplexer. In the multiplexer (Section III-B), as the PPW T-junctions have a wide bandwidth or can be designed to operate in dual bands, the achievable frequency ratios are essentially limited by the upper stopband of the LPF, the harmonic response of the BSF, and the effective signal path length in Diplexer 1(2) or 3 between the PPW T-junction output port and the cascaded LPF.

The upper stopband of the LPF can be improved by cascading multiple LPFs with different cut-off frequencies. However, the odd harmonic responses of the BSF, caused by the shorted stub (shown in Figs. 5 and 10), are hard to control. Assuming that f_1, f_2, and f_3 are the center frequencies of the three frequency bands from low to high. It would be difficult to achieve the frequency ratios of f_2 (or f_3) $/f_1 = n$ and $f_3/f_2=n$ (where n is an odd number greater than 1) without additional circuitry. The third harmonic response in Diplexer 1(2) can be

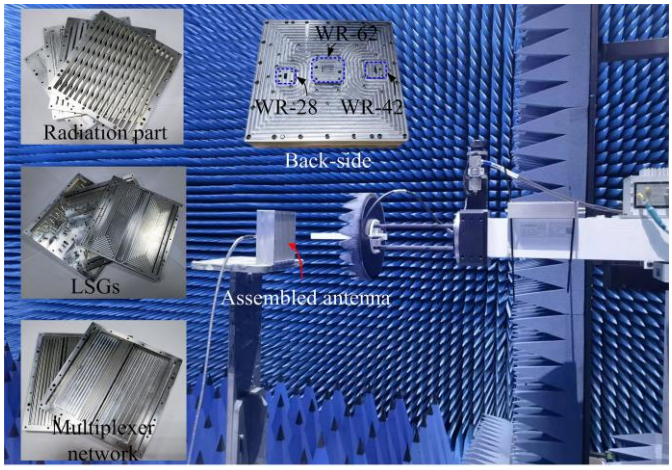

Fig. 19. Photographs of fabricated blocks, assembled antenna and test environment.

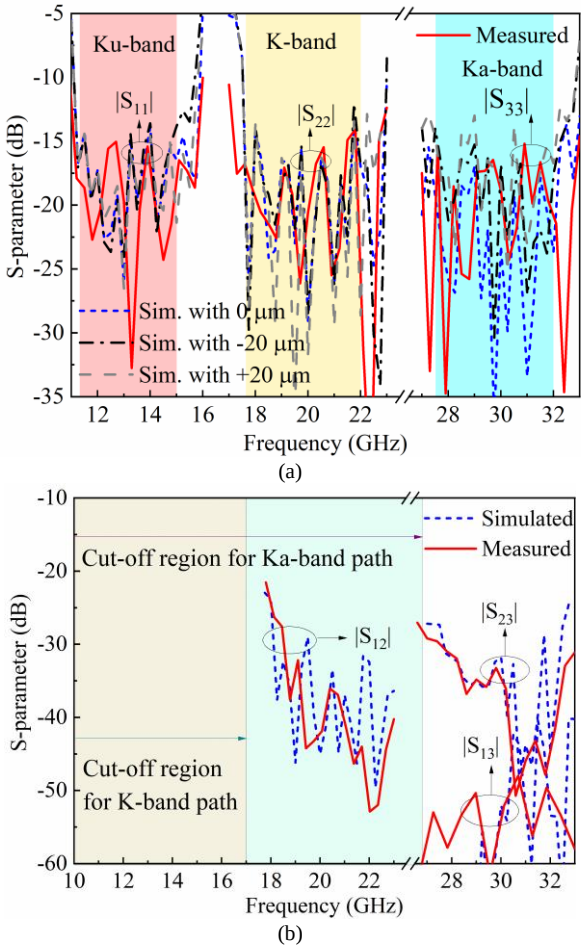

Fig. 20. Simulated and measured results. (a) Reflection coefficients; (b) isolation.

seen in Fig. 6(b). The bandstop characteristic appears at the third and even higher odd harmonics. Similar bandstop response also occurs in Diplexer 3.

Another critical dimension is the distance the between the PPW T-junction output port and the cascaded LPF, *dis*, as shown in Fig. 5. Reflection peak will appear at Port A in the upper stopband region, when this distance equals to $m \cdot \lambda/4$

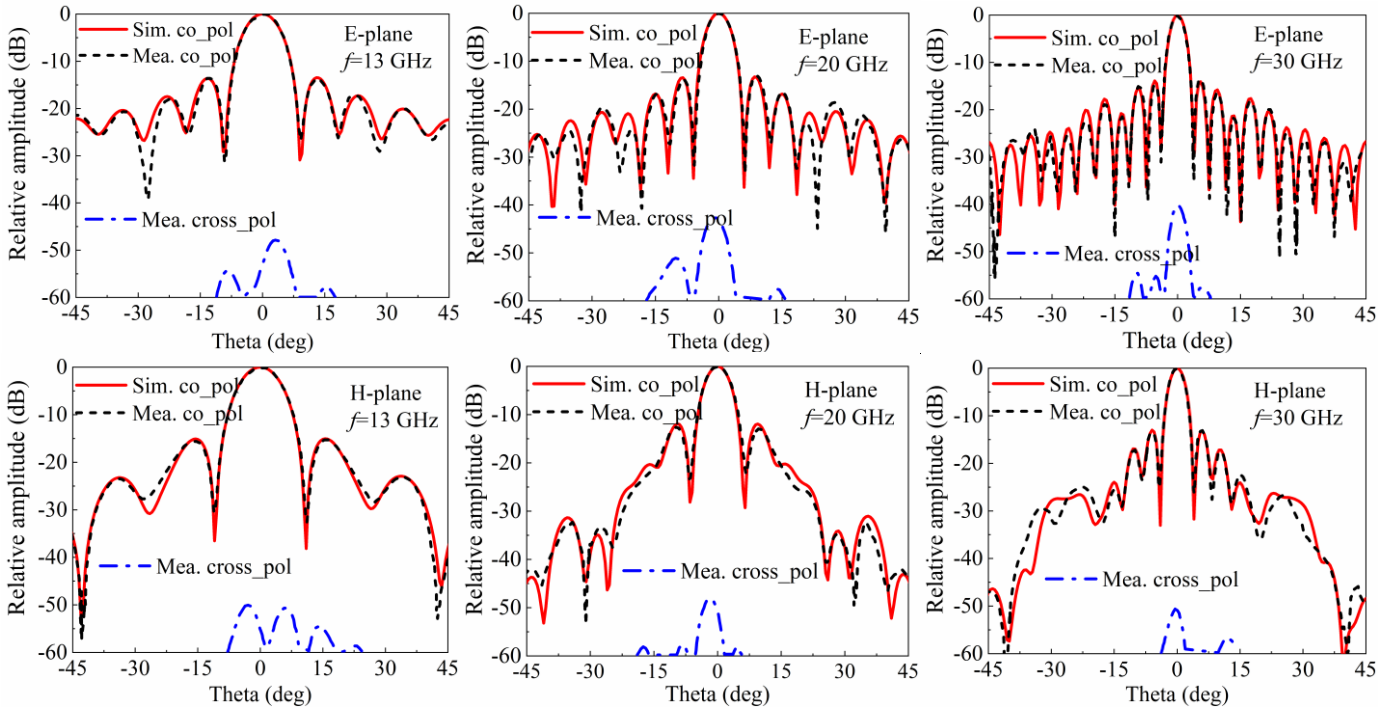

Fig. 21. Simulated and measured radiation patterns in E- and H-plane at different frequencies.

(where λ is the corresponding wavelength and *m* is an odd number) [43]. The antenna cannot be designed to operate at this frequency. Fig. 18 shows the simulated reflection coefficients in Diplexer 1 (2) with different values of *dis*. The reflection peak frequency varies with *dis*. It should be noted that the reflection peak in this figure corresponds to *m*=3. The same reflection characteristic also occurs in Diplexer 3. This must be considered in determining the achievable frequency ratios.

IV. Experimental Verification

As shown in Fig. 19, the radiation part, the PPW multiplexer and the LSGs are all divided into several layered blocks and fabricated by milling with a manufacture tolerance of 20 μm. Screws are used to assemble the antenna and suppress potential leakage. The overall size of the prototype is 158 mm × 150 mm × 51 mm (antenna aperture size: 150 mm × 142.4 mm). The measured reflection coefficients and isolations are taken from an Agilent E8361C network analyzer. A near-field planar scanner system (suitable for the test of directional antennas) from NSI-MI Technologies is used to record the antenna radiation performance in an anechoic chamber. The antenna performance in all three frequency bands is tested one by one. When one port was fed, the other ones are terminated with matched loads.

A. Reflection Coefficient and Isolation

Fig. 20 (a) shows the simulated and measured results, which are in a good agreement. It is noted that $|S_{11}|$, $|S_{22}|$ and $|S_{33}|$ are measured at the input ports for Ku-, K- and Ka-bands, respectively. The small difference is attributed to the assembly errors and fabrication tolerances. In the frequency range of 11.25-15 GHz, 17.7-22 GHz and 27.5-32 GHz (the FBW of 28.6%, 22%, and 15%), the simulated and measured reflection coefficients are both less than -12 dB. The potential influence from fabrication tolerance is also analyzed and reported in Fig. 20(a), which broadly confirms the contribution of fabrication tolerance to the performance variance. The measured isolations between input ports are plotted in Fig. 20(b). Due to the frequency cut-off characteristics of input waveguides for different frequency bands, Fig. 20(b) only shows the isolation in overlapping frequency bands between different ports. Both the simulated and measured isolations are better than 25 dB.

B. Radiation patterns and Efficiency

Fig. 21 shows the simulated and measured radiation patterns at different frequencies in the three bands. The measured results are very consistent with the simulations. The measured 3-dB beamwidths are 8.1°/9.2°, 5.3°/5.6°, and 3.5°/3.9° in E-/H-planes at 13 GHz, 20 GHz, and 30 GHz, respectively. The first lower SLLs are all around -13.2/-13.7 dB in E-/H- planes for all the three bands, which are consistent with first sidelobes characteristics of an array with a uniform amplitude excitation. The radiation pattern envelope outside of the range [-25°, 25°] in H-plane is lower than the one in E-plane. This is mainly because the amplitude of the quasi-TEM wave drops rapidly near the two ends of the radiation slot. The measured cross-polarization patterns are also shown in Fig. 21. It is less than -40 dB in the E- and H-planes.

The simulated and measured antenna efficiency and peak gain are plotted in Fig. 22 In the frequency range of 11.25–15 GHz, the measured peak gain varies from 24.7 to 27.5 dBi, while the simulated values are 25.1 - 27.7 dBi. In the other two bands of 17.7-22 GHz and 27.5-32 GHz, the simulated and measured peak gains are within the range of 28.6-30.8 / 28.2-30.5 dBi and 32.6-34.1 / 32.1-33.5 dBi, respectively. The difference between simulated and measured gains are mainly

TABLE II
PERFORMANCE COMPARISON OF MULTI-BAND SHARED-APERTURE ANTENNAS

Ref.	Antenna type	Number of slots	Center frequency (GHz)/ FBW (%)	Gain (dBi)	Antenna efficiency	SLL (dB)	XPD[1] (dB)	Isolation (dB)	Number of bands	Aperture size[2] (λ_0^2)
[18]	Microstrip line Fabry-Perot cavity + reflectarray antenna	--	8.9/11.2 25.3/10.0 37.5/13.3	16.8 23.8 26.7	>85%[3]	-18	>20	--	Triple bands	L[4]: 3×3 M: 8.4×8.4 H:12.5×12.5
[21]	SIW-based CTS LWA	15	77.6/3.4 89.7/14.5	27.1 25.3	49.1% 33.2%	--	35	40	Dual bands	L: 11.3×10.8 H: 13×12.6
[24]	GW-based slot antenna	4 × 4	20/10 30/10	16.6 18.5	83.3% 84.3%	--	30	50	Dual bands	--
[25]	GW-based slot antenna	8 × 8	20.5/10 30/6	25.9 29.3	82.1% 88.4%	--	30	40	Dual bands	L: 6.6×6.6 H: 9.6×9.6
[37]	HW-based ViCTS	15	19.8/3 29.3/2.7	24.2 28.5	-- --	-9	38	20	Dual bands	L: 7.3×6.5 H: 10.8×9.7
This work	HW-based CTS	16	13/28.6 20/21.7 30/15.1	>24.7 >28.2 >32.1	>84.5% >82.9% >80.5%	-13.2	>40	>25	Triple bands	L: 6.5×6.2 M: 10×9.5 H: 15×14.2

[1]XPD: Cross-polarization discrimination. [2]λ_0 is the free space wavelength at the center frequency of each passband. [3]Simulated radiation efficiency. [4]L: Low passband, M: Middle passband, H: High passband.

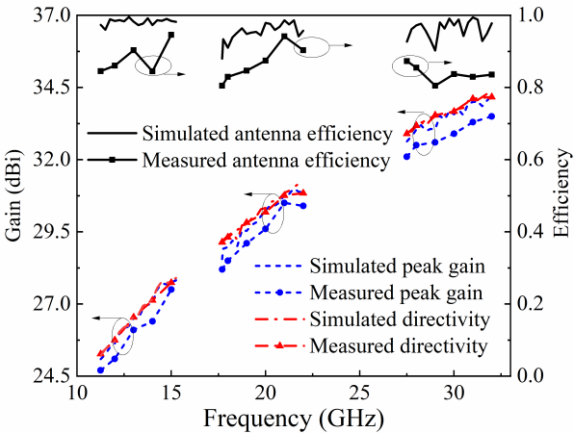

Fig. 22. Simulated and measured antenna peak gain and efficiency.

attributed to fabrication tolerances, assembly and measurement errors, as well as the slight energy leakage between the metal blocks. The measured directivities are 25.2-27.7 dBi, 29-30.8 dBi, and 32.9-34.1 dBi for the three frequency bands, respectively. Based on the measured peak gain and directivity, the measured antenna efficiencies are in the range of 84.5-94.6%, 82.9-94.2%, and 80.5-85.5% in the same three frequency bands. The measured aperture efficiencies in the three frequency bands are higher than 72%.

C. Comparison

Table II shows the performance comparisons between the proposed CTS antenna and other multi-band shared-aperture antennas. The works [18] and [21] are based on microstrip line and SIW, and others are based on HW. All these works are dual-band shared aperture antennas and no full-metal tri-band shared-aperture antenna reported. These HW-based dual-band shared aperture antennas of [24], [25] are slot array antennas using gap waveguide technology, while this work and [37] are CTS antenna based. [37] is a dual-band shared-aperture CTS antenna with a series-fed structure (that is, variable inclination CTS antenna), whereas this work adopts a full-corporate-feed tri-band shared-aperture CTS antenna. To the best of the authors' knowledge, this is the first HW-based tri-band shared-aperture antenna. A high antenna efficiency in all three frequency bands have been achieved.

D. Considering of polarization conversion

For satellite communications, circular polarization is often required, for example, in K- and Ka-bands (while it is linear polarization for Ku-band). To meet this requirement, the tri-band antenna considered in our work could be augmented by adding a multi-band or wideband polarization converter. There are two potential solutions. One is to use a linear-circular polarization combined multi-layer polarizer. By rotating the corresponding polarization layer, the required polarization may be achieved for different frequency bands. The basic principle was presented in [44]. Another approach is to integrate a Ku-band linear polarization function into K/Ka dual-frequency orthogonal circular polarizers. There have been several reports on dual-band circular polarizers [45], [46]. But these works did not consider the linear polarization of Ku-band. So, it remains an interesting challenge to implement a triple-band polarizer covering both linear and circular polarization.

V. CONCLUSION

In this paper, a Ku/K/Ka-band shared-aperture antenna was presented for the first time using CTS antenna technology. The tri-band operation was enabled by a novel and highly-sophisticated 6-port PPW multiplexer which defines the three bands, together with a broadband CTS radiation array and four separate wideband LSGs. Amplitude and phase pre-compensations were used to reduce the influence of the metal walls at the terminal ends of the PPW in the LSGs, thereby improving the radiation performance for three bands. Because of the wideband characteristics of the CTS radiator and the controllable frequency response of the multiplexer and separate line source generator, the frequency ratio of the shared-aperture antenna can be more flexibly adjusted. In spite of the complex structure of the antenna, the prototype has been successfully implemented using milling fabrication technique.

Simulation and measurement are consistent, verifying the design concept. This design provides a promising solution for multi-band wireless applications such as satellite and 5G millimeter-wave communications. A polarization converter covering the antenna can be used to obtain the desired polarization characteristics for different applications.

REFERENCES

[1] W. Hong et al., "The role of millimeter-wave technologies in 5G/6G wireless communications," *IEEE J. Microw.*, vol. 1, no. 1, pp. 101-122, Jan. 2021.

[2] V. Kuhn, C. Lahuec, F. Seguin and C. Person, "A Multi-band stacked RF energy harvester with RF-to-DC efficiency up to 84%," *IEEE Trans. Microw. Theory Techn.*, vol. 63, no. 5, pp. 1768-1778, May 2015.

[3] G. Kwon, J. Park, D. Kim and K. C. Hwang, "Optimization of a shared-aperture dual-band transmitting/receiving array antenna for radar applications," *IEEE Trans. Antennas Propag.*, vol. 65, no. 12, pp. 7038-7051, Dec. 2017.

[4] K. R. Mahmoud and A. M. Montaser, "Synthesis of multi-polarised upside conical frustum array antenna for 5G mm-Wave base station at 28/38 GHz," *IET Microw., Antennas Propag.*, vol. 12, no. 9, pp. 1559-1569, Jul. 2018.

[5] P. Naseri, S. A. Matos, J. R. Costa, C. A. Fernandes and N. J. G. Fonseca, "Dual-band dual-linear-to-circular polarization converter in transmission mode application to K/Ka-Band satellite communications," *IEEE Trans. Antennas Propag.*, vol. 66, no. 12, pp. 7128-7137, Dec. 2018.

[6] C. Granet, J. S. Kot and J. Ness, "Wideband Ka-band SATCOM-on-the-move antenna concept: preliminary design study," in *13th European Conference on Antennas and Propagation (EuCAP)*, Krakow, Poland, 2019, pp. 1-5.

[7] C.-X. Mao, S. Gao, Y. Wang, Q.-X. Chu, and X.-X. Yang, "Dual-band circularly polarized shared-aperture array for C − /X -band satellite communications," *IEEE Trans. Antennas Propag.*, vol. 65, no. 10, pp. 5171–5178, Oct. 2017.

[8] J. Wu, C. Wang and Y. X. Guo, "Dual-band co-aperture planar array antenna constituted of segmented patches," *IEEE Antennas Wireless Propag. Lett.*, vol. 19, no. 2, pp. 257-261, Feb. 2020.

[9] H. Ullah, F. A. Tahir and M. U. Khan, "Dual-band planar spiral monopole antenna for 28/38 GHz frequency bands," in *Proc. IEEE Int. Symp. Antennas Propag. USNC/URSI Nat. Radio Sci. Meeting*, San Diego, CA, 2017, pp. 761-762.

[10] Y. J. Cheng, J. Wang, and X. L. Liu, "94 GHz substrate integrated waveguide dual-circular-polarization shared-aperture parallel-plate long slot array antenna with low sidelobe level," *IEEE Trans. Antennas Propag.*, vol. 65, no. 11, pp. 5855–5861, Nov. 2017.

[11] Y. Liu, Y. J. Cheng, M. -H. Zhao and Y. Fan, "Dual-band shared-aperture high-efficiency reflectarray antenna based on structure-reuse technique," *IEEE Antennas Wireless Propag. Lett.*, vol. 20, no. 3, pp. 366-370, Mar. 2021.

[12] Y. Cai et al., "Dual-band circularly polarized transmitarray with single linearly polarized feed," *IEEE Trans. Antennas Propag.*, vol. 68, no. 6, pp. 5015-5020, June 2020.

[13] C.-X. Mao, S. Gao, Q. Luo, T. Rommel, and Q.-X. Chu, "Low-cost X/Ku/Ka-band dual-polarized array with shared aperture," *IEEE Trans. Antennas Propag.*, vol. 65, no. 7, pp. 3520–3527, Jul. 2017.

[14] Z. Sun, S. S. Zhong, L. B. Kong, C. Gao, W. Wang, and M. P. Jin, "Dual-band dual-polarised microstrip array with fractional frequency ratio," *Electron. Lett.*, vol. 48, no. 12, pp. 674–676, Jun. 2012.

[15] G. Jaworski, T. Maleszka, S. Gruszczynski, and K. Wincza, "Dual frequency & dual-linear polarization integrated Antenna array for application in synthetic aperture radar," in *Proc. 40th Eur. Microw. Conf.*, Paris, France, Sep. 2010, pp. 1714–1717.

[16] J.-D. Zhang, W. Wu, and D.-G. Fang, "Dual-band and dual-circularly polarized shared-aperture array antennas with single-layer substrate," *IEEE Trans. Antennas Propag.*, vol. 64, no. 1, pp. 109–116, Jan. 2016.

[17] P. H. Rao, S. Sujitha, and K. T. Selvan, "A multiband, mutipolarizatio shared-aperture antenna: Design and evaluation," *IEEE Antennas Propag. Mag.*, vol. 59, no. 4, pp. 26–37, Aug. 2017.

[18] P. Mei, X. Q. Lin, G. F. Pedersen and S. Zhang, "Design of a triple band shared aperture antenna with high figures of merit," *IEEE Trans. Antennas Propag.*, vol. 69, no. 12, pp. 8884-8889, Dec. 2021.

[19] Z. -J. Guo, Z. -C. Hao, H. -Y. Yin, D. -M. Sun and G. Q. Luo, "A planar shared-aperture array antenna with a high isolation for millimeter-wave low earth orbit satellite communication system," *IEEE Trans. Antennas Propag.*, vol. 69, no. 11, pp. 7582-7592, Nov. 2021.

[20] Y. Cheng and Y. Dong, "Dual-broadband dual-polarized shared aperture magnetoelectric dipole antenna for 5G applications," *IEEE Trans. Antennas Propag.*, vol. 69, no. 11, pp. 7918-7923, Nov. 2021.

[21] Y. -W. Wu, Z. -W. Miao, G. Q. Luo and Z. -C. Hao, "Planar millimeter-wave shared-aperture self-diplexing antenna with small frequency ratio and high isolation," *IEEE Trans. Antennas Propag.*, vol. 69, no. 12, pp. 8979-8984, Dec. 2021.

[22] Y. R. Ding and Y. J. Cheng, "Ku/Ka dual-band dual-polarized shared-aperture beam-scanning antenna array with high isolation," *IEEE Trans. Antennas Propag.*, vol. 67, no. 4, pp. 2413-2422, Apr. 2019.

[23] J. F. Zhang, Y. J. Cheng, Y. R. Ding and C. X. Bai, "A dual-band shared-aperture antenna with large frequency ratio, high aperture reuse efficiency, and high channel isolation," *IEEE Trans. Antennas Propag.*, vol. 67, no. 2, pp. 853-860, Feb. 2019.

[24] M. Ferrando-Rocher, J. I. Herranz-Herruzo, A. Valero-Nogueira and M. Baquero-Escudero, "Dual-band single-layer slot array antenna fed by K/Ka-band dual-mode resonators in gap waveguide technology," *IEEE Antennas Wireless Propag. Lett.*, vol. 20, no. 3, pp. 416-420, Mar. 2021.

[25] M. Ferrando-Rocher, J. I. Herranz-Herruzo, A. Valero-Nogueira and B. Bernardo-Clemente, "Full-metal K-Ka dual-band shared-aperture array antenna fed by combined ridge-groove gap waveguide," *IEEE Antennas Wireless Propag. Lett.*, vol. 18, no. 7, pp. 1463-1467, Jul. 2019.

[26] Y. Gao, T. Hong, W. Jiang, S. Gong and F. Li, "Low-profile wideband CTS array using substrate-integrated waveguide technology for K-band applications," *IEEE Trans. Antennas Propag.*, vol. 67, no. 8, pp. 5711-5716, Aug. 2019.

[27] T. Potelon, M. Ettorre and R. Sauleau, "Long slot array fed by a nonuniform corporate feed network in PPW technology," *IEEE Trans. Antennas Propag.*, vol. 67, no. 8, pp. 5436-5445, Aug. 2019.

[28] Y. Lu, Q. You, Y. Wang, Y. You, J. Huang and K. Wu, "Millimeter-wave low-profile continuous transverse stub arrays with novel linear source generators," *IEEE Trans. Antennas Propag.*, vol. 67, no. 2, pp. 988-997, Feb. 2019

[29] Q. You, Y. Lu, Y. You, Y. Wang, Z. Hao and J. Huang, "Wideband full-corporate-feed waveguide continuous transverse stub antenna array," *IEEE Access*, vol. 6, pp. 76673-76681, 2018.

[30] F. Foglia Manzillo et al., "A wide-angle scanning switched-beam antenna system in LTCC technology with high beam crossing levels for V-band communications," *IEEE Trans. Antennas Propag.*, vol. 67, no. 1, pp. 541-553, Jan. 2019.

[31] H. Qiu, X. Yang, Y. Yu, T. Lou, Z. Yin and S. Gao, "Compact beam-scanning flat array based on substrate-integrated waveguide," *IEEE Trans. Antennas Propag.*, vol. 68, no. 2, pp. 882-890, Feb. 2020.

[32] X. Lu, S. Gu, X. Wang, H. Liu and W. Lu, "Beam-scanning continuous transverse stub antenna fed by a ridged waveguide slot array," *IEEE Antennas Wireless Propag. Lett.*, vol. 16, pp. 1675-1678, 2017.

[33] K. Tekkouk, J. Hirokawa, R. Sauleau and M. Ando, "Wideband and large coverage continuous beam steering antenna in the 60-GHz band," *IEEE Trans. Antennas Propag.*, vol. 65, no. 9, pp. 4418-4426, Sep. 2017.

[34] Y. You, Y. Lu, Y. Wang, J. Xu, J. Huang and W. Hong, "Enhanced pencil-beam scanning CTS leaky-wave antenna based on meander delay line," *IEEE Antennas Wireless Propag. Lett.*, vol. 20, no. 9, pp. 1760-1764, Sept. 2021.

[35] X. Yang, L. Di, Y. Yu and S. Gao, "Low-profile frequency-scanned antenna based on substrate integrated waveguide," *IEEE Trans. Antennas Propag.*, vol. 65, no. 4, pp. 2051-2056, Apr. 2017.

[36] M. Del Mastro, A. Mahmoud, T. Potelon, R. Sauleau, G. Quagliaro and M. Ettorre, "Low-profile CTS array in PCB technology for K/Ka-band applications," in *15th European Conference on Antennas and Propagation (EuCAP)*, Dusseldorf, Germany, 2021, pp. 1-3.

[37] R. S. Hao, Y. J. Cheng and Y. F. Wu, "Shared-aperture variable inclination continuous transverse stub antenna working at K- and Ka-band for mobile satellite communication," *IEEE Trans. Antennas Propag.*, vol. 68, no. 9, pp. 6656-6666, Sep. 2020.

[38] F. Foglia Manzillo, M. Ettorre, M. Casaletti, N. Capet, and R. Sauleau, "Active impedance of infinite parallel-fed continuous transverse stub array," *IEEE Trans. Antennas Propag.*, vol. 63, no. 7, pp. 3291-3297, Jul. 2015.

[39] M. Samardzija, T. Kai, J. Hirokawa and M. Ando, "Single-layer waveguide feed for uniform plane TEM-wave in oversized-rectangular waveguide with hard-surface sidewalls," *IEEE Trans. Antennas Propag.*, vol. 54, no. 10, pp. 2813-2819, Oct. 2006.

[40] J. Hirokawa and M. Ando, "Efficiency of 76-GHz post-wall waveguide-fed parallel-plate slot arrays," *IEEE Trans. Antennas Propag.*, vol. 48, no. 11, pp. 1742-1745, Nov. 2000.

[41] L. Qin, Y. Lu, Q. You, Y. Wang, J. Huang and P. Gardner, "Millimeter-wave slotted waveguide array with unequal beamwidths and low sidelobe levels for vehicle radars and communications," *IEEE Trans. Veh. Technol.*, vol. 67, no. 11, pp. 10574-10582, Nov. 2018.

[42] J. Hirokawa and M. Ando, "Sidelobe suppression in 76-GHz post-wall waveguide-fed parallel-plate slot arrays," *IEEE Trans. Antennas Propag.*, vol. 48, no. 11, pp. 1727-1732, Nov. 2000.

[43] M. Zhang, J. Hirokawa and M. Ando, "A four-corner-fed double-layer waveguide slot array with low sidelobes developed for a 40 GHz-band DDD system," *IEEE Trans. Antennas Propag.*, vol. 64, no. 5, pp. 2005-2010, May 2016.

[44] W. W. Milroy *et al.*, "Wide-scan-capable polarization-diverse polarizer with enhanced switchable dual-polarization properties," U.S. Patent 0151901 A1, May 20, 2021.

[45] M. Del Mastro, M. Ettorre and A. Grbic, "Dual-band, orthogonally-polarized LP-to-CP converter for SatCom applications," *IEEE Trans. Antennas Propag.*, vol. 68, no. 9, pp. 6764-6776, Sep. 2020.

[46] E. Arnieri, F. Greco, L. Boccia and G. Amendola, "A SIW-based polarization rotator with an application to linear-to-circular dual-band polarizers at K-/Ka-Band," *IEEE Trans. Antennas Propag.*, vol. 68, no. 5, pp. 3730-3738, May 2020.